

ORIGINAL PAPER

Open Access



Genesis of host rock in the Tamusu Mudstone pre-selected area in Northwest China for high-level radioactive waste geological disposal purposes

Long Xiang^{1,2}, Xiaodong Liu^{1,2}, Pinghui Liu^{1,2*}, Chaocheng Dai^{1,2} and Meixia Jiang^{1,2}

Abstract

Mudstone characterized by typical structures and mineral assemblages in the Tamusu Mudstone pre-selected area, in Inner Mongolia, Northwest China, has been selected as a potential host rock for China's high-level radioactive waste (HLW) repository purpose. Based on indications of petrological and geochemical characteristics, hydrothermal sedimentary geneses of host rock are well discussed from the perspectives of hydrothermal sedimentary structures, sedimentary environments, and the hydrothermal sedimentary model. The results show that host rocks have the characteristics of low-temperature "white smoke" hydrothermal sedimentary rocks. The rocks developed in a dry, anaerobic and reducing saline lake environment with transient oxidation and dry–wet evolution. The 100–120 Ma tectonic activity in the Altun fault may have been the main factor controlling the process of hydrothermal exhalative, which provided the migration pathway for water–rock reactions and contributed to the formation of typical structures and mineral assemblages. The hydrothermal sedimentary rock is a new kind of argillaceous rock that serves as a potential host rock, and will provide new insights into suitability evaluations of mudstone properties to promote the site screening of the Tamusu Mudstone pre-selected area for China's HLW disposal purpose.

Keywords Host rock genesis, Hydrothermal sedimentary rock, Tamusu Mudstone pre-selected area, HLW geological disposal

1 Introduction

As one of the essential parts of multi-barrier systems for the permanent disposal of high-level radioactive waste (HLW), host rock (as a natural geological barrier) plays a critical role in ensuring the long-term safety of deep geological repositories (DGRs) (IAEA, 2003; Pan & Qian,

2009; SKB, 2004). Currently, crystalline rocks and argillaceous media are the two principal types of host rocks that are considered worldwide (Faybishenko et al., 2017). Argillaceous media (Clay rocks, mudstone, shales, etc.) are widely accepted as potential host rock due to their attractive properties, such as large rock masses, stable geological structures, low hydraulic conductivity, self-sealing potential of fractures and high sorption capacity for radionuclides (Bossart et al., 2017; Zhang, 2018).

On the Chinese mainland, the Beishan granite (in Northwest China's Gansu Province) was preselected as a potential host rock for HLW repository purposes (Wang et al, 2018a), and an underground research laboratory (URL) has been under construction at the

Editorial handling: Wilfried Winkler

*Correspondence:

Pinghui Liu
pinghui_liu@126.com

¹ State Key Laboratory of Nuclear Resources and Environment, East China University of Technology, Nanchang 330013, China

² School of Earth Sciences, East China University of Technology, Nanchang 330013, China

Xinchang Site since June 17, 2021 (CAEA, 2021). Moreover, based on the China's "Guidelines for the R&D for Geological Disposal of HLW", an argillaceous-based site should also be considered in site selection research in addition to the granite-based sites. The Tamusu pre-selected area in Inner Mongolia, Northwest China, is in an arid desert zone, and has a typical temperate continental climate; it is generally divided into four types: Gobi (50%), desert (30%), and mountains and hills (20%). The Tamusu area is approximately 24,327 km² in total, and according to a 2015 survey data analysis, the permanent population is 1594, with an extremely low population density of 0.07 people/square kilometer. The permanent population exceeds only 1.1% of the townships in the whole country. The economic strength of the Tamusu area is higher than only 11.8% of the townships in the whole country, highlighting the low population density and relatively underdeveloped economic level. As one of argillaceous-based site working areas, the Tamusu Mudstone has been selected as a potential host rock for China's HLW repository. Preliminary work has confirmed that Tamusu Mudstones are mainly composed of dolomite and analcime, and the clay mineral content accounts for only approximately 10%. The main minerals are distinct from traditional clay stones that are used for HLW disposal purposes, such as the Callovo-Oxfordian (COX) clay in France and the Opalinus (OPA) clay in Switzerland (Xiang et al., 2020). However, the sedimentological and geochemical characteristics of the Tamusu Mudstone indicates the abnormal deposition process and the depositional environment and model are still unclear. In particular, the geneses of analcime and dolomite should be further explored, as these geneses play important roles in determining the rock property parameters, such as the sorption potential and mechanical properties. Because the site screening project is progressing, the genesis of the Tamusu Mudstone should be solved first to promote suitability evaluations on the suitability of the host rock in the Tamusu pre-selected area.

In this paper, the structural and geochemical characteristics of the Tamusu Mudstone are described in detail. Then, the hydrothermal sedimentary geneses are determined. Third, the structure of hydrothermal sedimentary rock, main mineral geneses, sedimentary environment and hydrothermal sedimentary model are thoroughly discussed. Finally, the basic performances of hydrothermal sedimentary rocks as potential host rocks are preliminarily analyzed. This study will lay solid foundations to suitability evaluations on the Tamusu Mudstone and to promote site screening in the Tamusu pre-selected area.

2 Geological background

2.1 The Bayingebi Basin

The Tamusu pre-selected area is located in the middle-southern part of the Alxa Block and the northeast margin of the Yingejing Sag, Bayingebi Basin, Northwest China (Fig. 1A). The horizontal stresses in the Alxa Block are at an intermediate or low level. The maximum horizontal stress in the Alxa Block is dominantly oriented in the NNE-SSW direction, which is consistent with the direction of the tectonic stress field of Northwest China (Du et al., 2017; Rao et al., 2021). Bayingebi Basin is located on the southern margin of the Xingmeng Orogenic Belt (Lin et al., 2001; Dou & Chang, 2003; Zhang et al., 2019) in the Eastern Central Asian Orogenic Zone (Zhou et al., 2011), which is framed by the Siberian Craton and the North China Craton (Fig. 1A) (Charles et al., 2013). The Yingejing Sag is located in the southern extremity of Bayingebi Basin and the southeastern margin of the Altun Fault, extending in a northeast direction. The northern margin of the sag is adjacent to the Zongnaishan-Salaza uplift, the southern margin is adjacent to the Bayanorgong uplift, and the eastern margin is adjacent to the Yingen Sag (Fig. 1B).

The formation and evolution of the Bayingebi Basin has undergone fundamental changes since the Mesozoic. Since the Triassic, the tectonic evolution of the Bayingebi basin has been mainly divided into the following four stages. (1) The first stage was generation of the Triassic-Jurassic pull-apart basin. Affected by the Indosinian movement, the basin was uplifting in the Early Triassic. In the Late Triassic, the basin entered the post-orogenic extensional relaxation stage, and the surface of the crust exhibited tensional tectonic conditions, forming a group of NE tensional tectonic systems. During the Jurassic period, due to the strike-slip action of the Altun fault, the basin developed NE and NE fault systems based on the basement fault, and the extensional fault developed in the Triassic; as a result, the basin is similar to a graben basin. (2) The second stage was the comprehensive development of the Early Cretaceous pull-apart basin. In the Early Cretaceous, affected by the continuous strike-slip of the Altun fault and its branch faults, the basin entered the stage of comprehensive development of the pull-apart basin. The northern sags further expanded on the basis of inheritance. The southern sags are controlled by the large regional fault, with tensional and torsional properties, showing the same trend as the Altun fault and its branches. (3) The third stage was the Late Cretaceous extensional depression stage. In the Late Cretaceous, regional rifting weakened as the volcanic eruptions declined. The regional compensation caused the sag to form in a larger area than that of the rift, and the basin shows overall sag subsidence. (4) The fourth stage was the

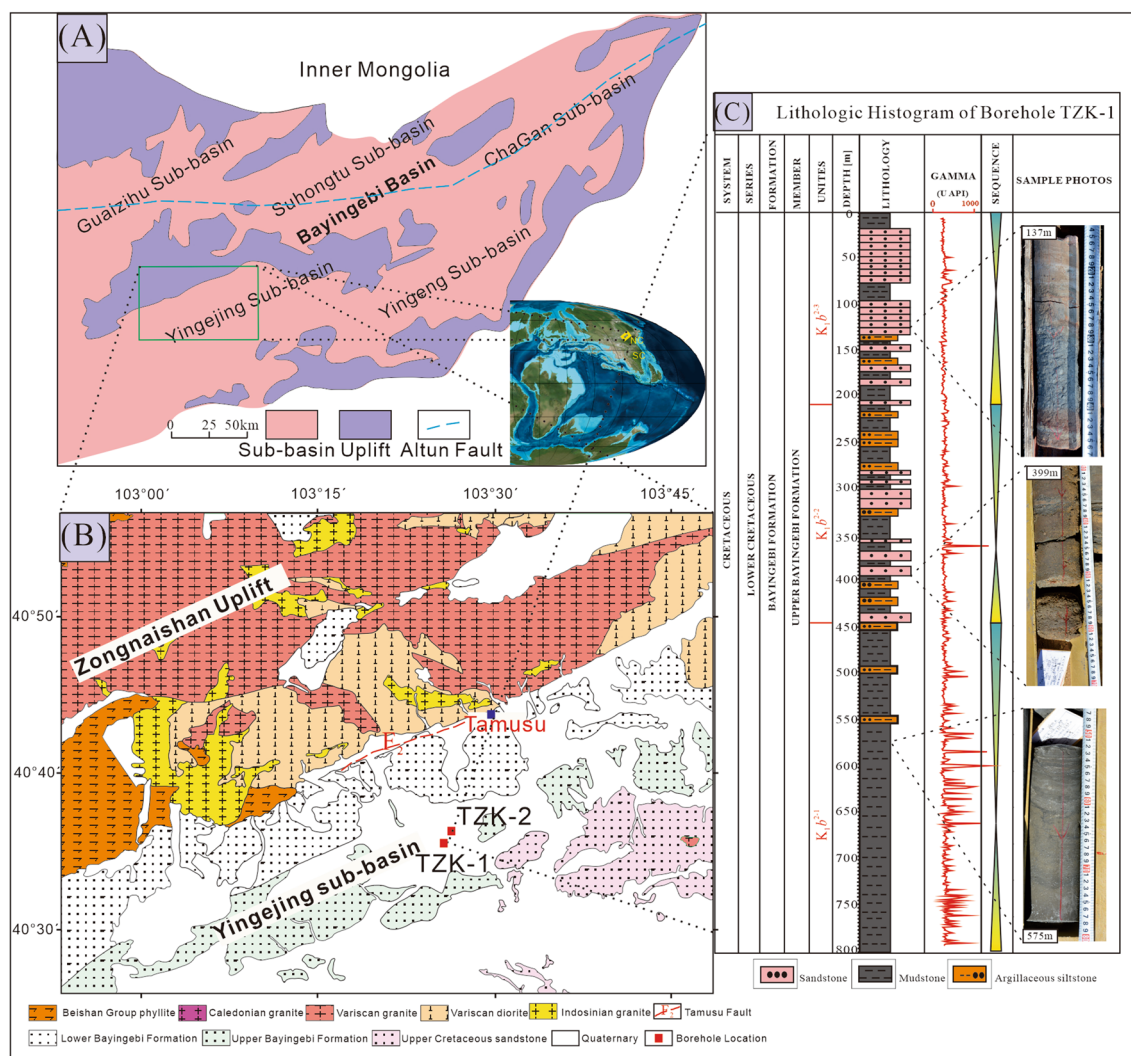


Fig. 1 Location of Yingjing Sag and lithologic histogram of TZK-1 (Xiang et al., 2020; Wei & Jiang, 2019) A The Location of the Yingjing Sag; B The Locations of the Tamusu Mudstone pre-selected area and the drilled boreholes; C the lithologic histogram of TZK-1

Palaeogene intracontinental convergence stage. Under the influence of collision between the Indian plate and the Eurasian plate, the tectonic stress field of the basin changed from extensional to compressive stress, making the basin a tectonic setting of compressional uplift during this period.

Overall, the Altun fault zone has controlled the overall structural pattern of uplifts and depressions in the basin evolutionary process. The Tamusu pre-selected area widely received Lower Cretaceous sediments, including the lower part of the Bayingebi Formation and the upper part of the Bayingebi Formation during the Early Cretaceous in the stage of development of the pull-apart basin. In the late Early Cretaceous, structural inversion caused the upper part of the Bayingebi Formation to be directly uplifted and exposed to the surface. Since the neotectonic

movement, the surface of the Tamusu pre-selected area has been extensively covered by Quaternary aeolian sand and gravel, forming its current appearance.

2.2 The target formation

The basement of the Yingjing Sag is composed of Archean, Proterozoic and Palaeozoic metamorphic rocks, which are overlain by Jurassic and Cretaceous sedimentary rocks, as well as Quaternary sediments. The Early Cretaceous strata could be divided into the lower Bayingebi Formation (K_1b^1) and the upper Bayingebi Formation (K_1b^2). The lithology of unit lower Bayingebi Formation is mainly purple-red conglomerate and sandstone with occasional siltstone and mudstone, and its maximum burial depth is approximately 1400 m. The upper Bayingebi Formation (K_1b^2) is the target formation,

which consists of a succession of mudstone-sandstone-mudstone and has a maximum depth of ~911 m (Wang et al., 2018b). The two sections of lacustrine mudstone with continuous thicknesses of more than 100 m are key research objects for host rock considerations. In particular, taking borehole TZK-1 as an example, the first unit with a maximum depth of ~200 m consists primarily of fine-grained sandstone and silty mudstone, which were deposited in a semi-deep to deep lacustrine environment. The second unit (200–450 m) is composed mainly of yellowish-brown sandstone, siltstone, and grey mudstone, representing fan delta and braided delta plain sub-facies. The third unit (450–800 m) consists of dark grey mudstone, which formed in a semi-deep to shallow lacustrine environment (Fig. 1C).

3 Materials and methods

The collected boreholes from the Tamusu pre-selected area were carried out with water by single core barrel-ling techniques. Core samples from TZK-1 and ZK-2 were vacuum sealed to maintain freshness. Core samples from ZHK88-15, ZKH104-8 were provided by the Geological Team No. 208, CNNC. A total of 116 whole-mudstone samples from borehole TZK-2 were used for Conventional X-ray diffraction (XRD) analyses (D8 ADVANCE, Bruker, Germany). XRD analysis was carried out on whole-rock powdered samples with Cu-K α radiation operating at 40 mA and 40 kV, and diffraction traces were recorded from 5 to 70°2 θ and the semi-quantitative estimates of relative mass fractions were calculated using the Bruker Diffrac.EVA package. 7 mudstone samples from ZHK88-15, TZK-1, TZK-2 and ZKH104-8 were prepared for scanning electron microscope (SEM) tests (Nova NanoSEM 450, Czech Republic) and electron probe microanalysis (EPMA) tests (JXA-8530F Plus, Japan). The EPMA analytical conditions were as follows: an acceleration voltage of 15 kV, a current of 20 nA, and a beam spot diameter of <2 μ m, with a 10 s counting time for the major elements, and 20 s or 40 s for the minor elements. The above-mentioned tests were completed in the State Key Laboratory of Nuclear Resources and Environment, East China University of Technology, China. 30 mudstone samples from borehole TZK-2 were tested for geochemical analyses (rare earth elements (REEs), trace elements and main elements) (ICP-AES, Agilent, America; ICP-MS, Perkin Elmer Elan 9000, America) that were completed by ALS Chemex (Guangzhou) Co Ltd, China. The accuracy and precision (relative deviation and relative error) of the detection method are controlled within 10 (\pm 5)%.

4 Results

4.1 Sedimentological characteristics of host rock

4.1.1 Mineral composition

Based on the whole-rock mineralogical analysis of 116 samples, the mass fractions of dolomite and ankerite range from 3 to 50% and from 4 to 25%, with average mass fractions of 28% and 13%, respectively. The mass fractions of analcime and calcite range from 1 to 43% and from 0.2% to 23%, with averages of 17% and 3%, respectively. The mass fractions of albite, quartz, hematite and pyrite are evenly distributed and range from 7 to 40%, 1 to 11%, 1 to 9% and 2 to 20%, with average values of 19%, 5%, 4% and 6%, respectively. The mass fractions of illite and kaolinite range from 2 to 6% and from 1 to 4%, with average mass fractions of 3% and 2%, respectively. Vertically, three facies could be distinguished (Fig. 6). The first facies (381.82–528.77 m, above Line E–F) is composed mainly of analcime, carbonate minerals and albite, with analcime being the most abundant. The second facies (528.77–723.79 m, between Line E–F and Line M–N) consists mainly of carbonate minerals, analcime and albite. The third facies (723.79–800.06 m, below Line M–N) is composed mainly of carbonate minerals and albite, showing the smallest analcime content. Notably, the host rock in the Tamusu pre-selected area is characterized by analcime and dolomite and could be defined as mudstone rather than traditional clay stone.

4.1.2 Mineral paragenesis

According to detailed thin-section observations and XRD analysis, four kinds of mineral assemblages in mudstone are present: I) dolomite–ankerite–analcime–albite; II) dolomite–ankerite–analcime–albite–quartz; III) dolomite–ankerite–albite–quartz–gypsum; IV) dolomite–ankerite–albite–quartz–pyrite. The relationships between paragenetic sequences and tectonic events are constructed in Fig. 2.

In the syn-sedimentary stage, the sandstone is immature, and detrital grains consist of quartz, feldspar, and rock fragments. Then, the structural inversion of the basin results in the oxidation stage, which occurs mainly at the contact between the oxidized sandstone and gray sandstone. The active phase of the Altun fault that occurred at 100–120 Ma indicates that a hydrothermal event occurred and provided a migration channel for the ascent of deep hydrothermal fluids (Zuo et al., 2015; Zhang et al., 2020). The host rock has undergone significant alteration during the hydrothermal activity stage, which is mainly manifested by the recrystallization and

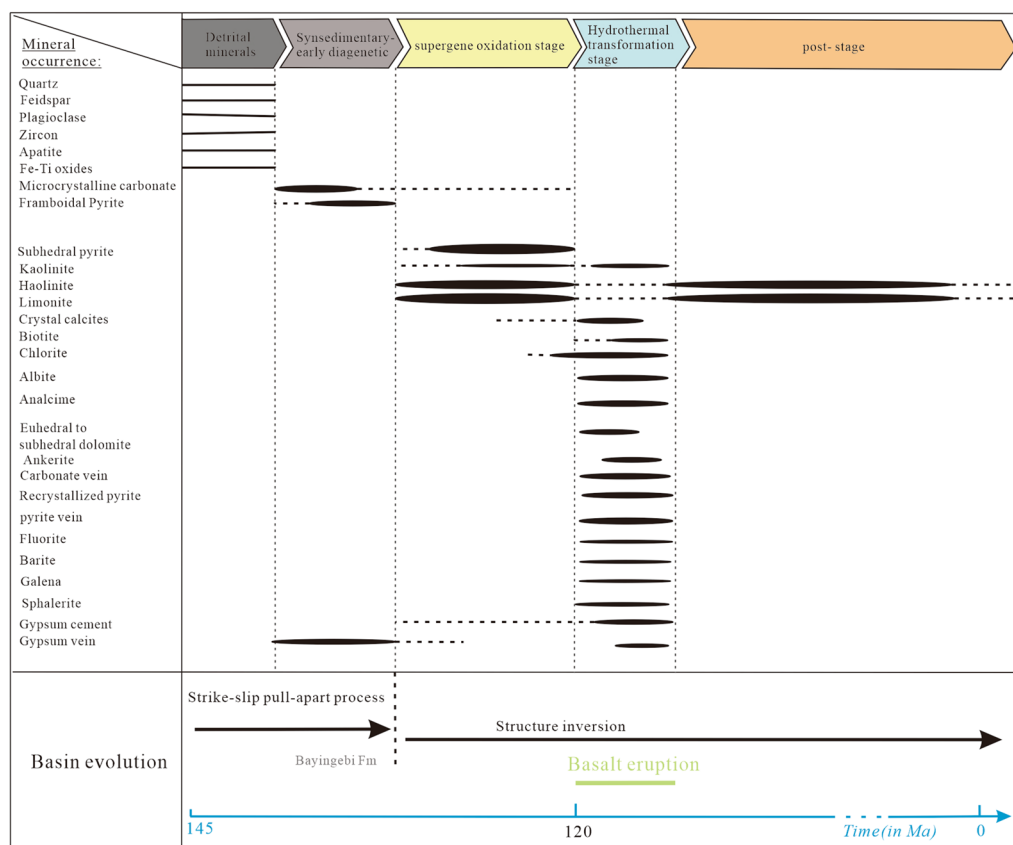


Fig. 2 Relationship between paragenetic sequences and tectonic events in Tamusu pre-selected area (after Zhang et al., 2019)

formation of new minerals. The recrystallization of carbonate, analcime and plate-like pyrite is widely distributed, which contributes to the formation of euhedral and subhedral coarse-grained carbonate minerals, analcime and cubic pyrite. A large number of fine dolomite and ankerite crystals are distributed along the edges or in the pores between detrital grains, forming the mud-supported texture. The hydrothermal event caused a general consolidation of the sandstone and mudstone in the post-stage via the cementation of carbonate and gypsum (Zhang et al., 2019).

4.1.3 Sedimentary structure

A number of borehole cores derived from boreholes TZK-1 and 2 (for the locations, see Fig. 1b) show that host rocks are mainly dark gray and gray-white, and they feature five kinds of typical sedimentary structures, i.e., the network vein filling, mud-supported, massive, laminar and syngenetic deformation structures (Fig. 3).

The network vein filling structures generally crosscut host rock and characterized by white thick strips with widths varying from 1 to 8 mm (Fig. 3a). The white network is mainly composed of dolomite, analcime

and microcrystalline calcite mixed with dark argillaceous matter (Fig. 3b). The mud-supported structures are observed as "snowflakes" distributed in dark gray mudstone (Fig. 3c). The coarse-grained dolomite is determined by typical rhombohedral crystal forms with sizes ranging from 0.5 mm to 1 mm (Fig. 3d). The laminar structure is one of common sedimentary structures, and an increase in lamina thickness to the millimeter or even centimeter level is called a banded structure (Fig. 3e). The laminae are mainly composed of powder-fine dolomite, ankerite and analcime (Fig. 3f). The contemporaneous deformation structures are well developed based on soft deformation and irregular ruffled bedding structures. As the main structural type of host rock, the massive structure is characterized by grey and dark grey mudstone with good homogeneity and a high degree of consolidation (Fig. 3g).

4.2 Elemental geochemistry

The percentages of major elements are shown in Table 1. More than 60% of the oxides in the samples are composed of SiO₂ (avg. 33.18%), CaO (avg. 12.17%), Al₂O₃ (avg. 11.09%), MgO (avg. 7.58%), and TFe₂O₃ (avg. 4.72%).

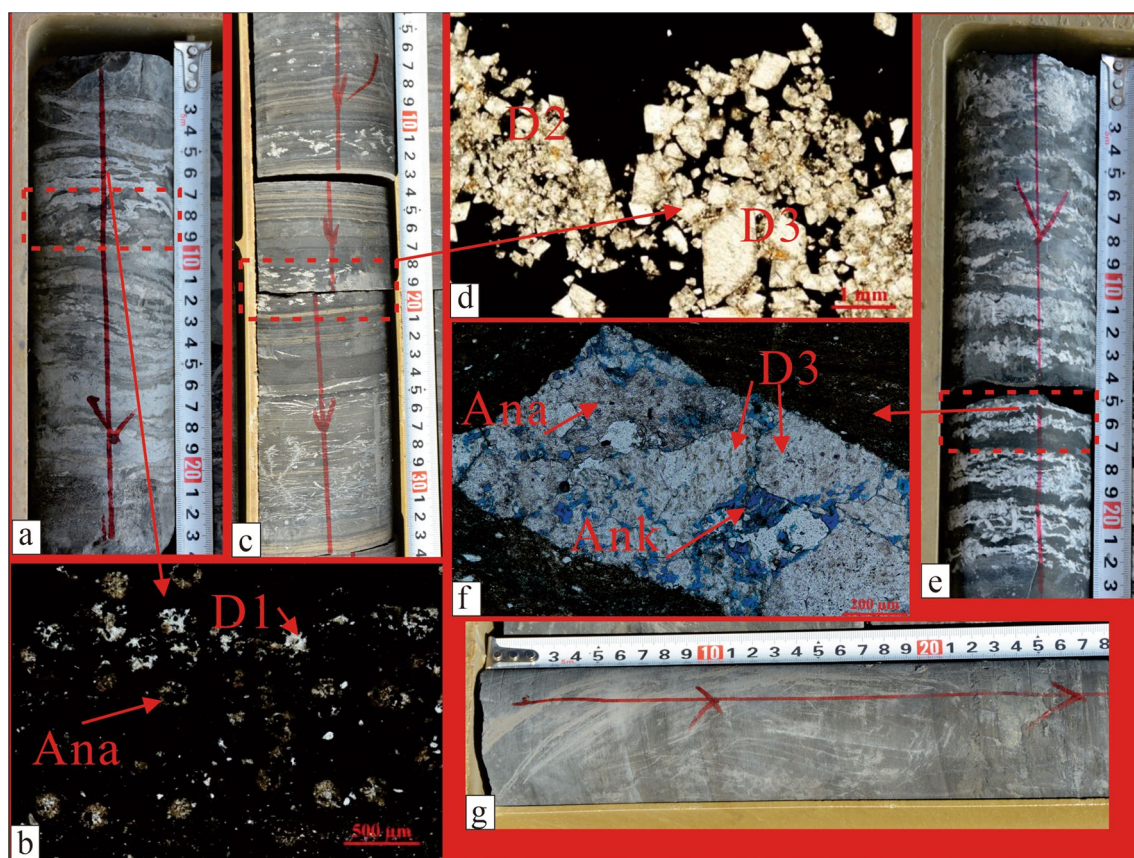


Fig. 3 Sedimentary structures of host rock in Tamusu pre-selected area. **a** The network vein filling structures, the marked white network is composed of analcime, clay minerals and dolomite, Borehole TZK-2, 765 m; **b** dark argillaceous minerals mixed with analcime and powder-fine dolomite, single polarization light; **c** “matrix-supported” structure, the marked white matrix are powder-fine-grained and coarse-grained dolomite, Borehole TZK-1, 595 m; **d** rhombic coarse-grained dolomite and powder-fine-grained dolomite are distributed in dark argillaceous minerals, single polarization light; **e** white and grey-white laminae developed in the dark grey mudstone; **f** the marked area is composed of dolomite, ankerite and analcime, Borehole TZK-2, 137 m, dyed thin section, single polarization light; **g** grey massive mudstone, Borehole TZK-1, 520 m; D1: mud-micro dolomite; D2: powder-fine dolomite; D3: coarse-grained dolomite; Ana: analcime; Ank: ankerite

The relatively high concentrations of loss on ignition (LOI) (avg. 20.77%), MgO and CaO confirm that the mudstone contains dolomite. The total combined content of TiO_2 , P_2O_5 and MnO accounts for approximately 1% of the total oxides. Taking the average content of major elements in the upper continental crust (UCC) as the standard (Fig. 4a) (Taylor & McLennan, 1985), host rock is enriched in Ca, Na and Mn, and relatively depleted in K and P.

The concentrations of trace elements are shown in Table 1. The calculated concentration coefficients display high enrichments in U, Sr, and V; and depletions in Ba, Rb, Sc, Th, and Zr (Fig. 4b). The abundance of typical deep-source gas–liquid trace Sr is up to 274 ppm. Compared with typical hydrothermal sedimentary areas in the Shahejie Formation and the Xiagou Formation, North

China, trace elements show a consistently changing trend (Table 2, Fig. 4c).

The concentrations of rare earth elements (REEs) are shown in Table 1. The total concentration of REEs is 59.29–283.80 ppm (avg. 139 ppm). The ratio difference between light REEs (LREEs) and heavy REEs (HREEs) is more than 20 times, which further confirms the enrichment of LREE and deficiency of HREEs (Fig. 4d). The δCe (0.91–1.04, avg. 1.01) indicates a weak negative anomaly, while the δEu (0.55–0.70, avg. 0.62) shows a moderately strong deficit. REEs have characteristics of higher totals, enrichment in LREEs, depletions in HREEs, and strong positive δEu anomalies, which are different from marine hydrothermal sedimentary rocks (HREEs are higher than LREEs, and δEu anomalies are positive) (Klinkhammertal et al., 1994; Zheng et al., 2018; Zhong et al., 2018).

Table 1 Main geochemical characteristics of the Tamusu hydrothermal-sedimentary rock

NO	Depths/m	SiO ₂	CaO	Al ₂ O ₃	MgO	TFe ₂ O ₃	K ₂ O	Na ₂ O	P ₂ O ₅	TiO ₂	LOI 1000	Ni	Co	Rb	Ba	Sr	V	Th	U	Sc	Zr	Cu					
T41	381.82	40.44	8.70	14.48	5.55	6.26	2.66	4.71	0.14	0.60	15.26	33.40	19.7	122.00	375	650	134	13.60	11.20	13.80	80	45.90					
T44	398.65	39.09	10.45	13.18	6.23	5.67	2.72	4.18	0.21	0.60	16.16	26.40	17.6	129.50	337	949	176	19.10	24.10	13.10	81	43.10					
T52	427.17	32.58	14.80	10.66	7.62	5.25	2.27	3.37	0.13	0.49	21.85	22.60	14.4	103.00	325	1155	158	12.00	16.0	11.90	61	34.40					
T55	440.08	33.97	13.60	11.01	7.68	4.77	2.49	3.49	0.50	0.47	19.91	26.60	14.2	122.00	188	1330	201	14.45	85.1	10.80	62	36.30					
T58	451.71	40.19	7.56	14.80	5.53	6.46	2.23	5.63	0.11	0.62	16.01	27.80	18.5	119.50	276	539	153	10.85	8.40	15.40	62	42.40					
T59	454.9	49.62	3.38	18.84	2.54	4.04	2.94	7.16	0.16	0.90	9.51	37.50	20.9	171.00	458	679	159	15.00	5.4	12.60	90	55.60					
T60	458.11	27.17	18.40	8.03	9.76	3.64	2.08	2.54	0.63	0.34	26.00	18.70	11.7	98.30	159	1720	139	9.73	73.30	9.30	53	27.60					
T61	461.9	38.75	8.27	14.42	5.80	6.49	2.28	5.40	0.09	0.59	17.24	24.50	15.7	122.50	282.0	739	156	10.40	6.8	15.20	63	41.40					
T66	483.82	44.63	5.13	15.83	3.98	6.22	2.97	5.92	0.09	0.71	11.91	27.00	18.0	145.00	269	595	141	7.87	5.70	12.20	72	44.00					
T70	496.75	44.18	5.19	16.75	4.10	3.92	2.74	6.77	0.10	0.70	14.13	19.20	12.6	136.50	265.0	526	131	8.03	5.9	11.40	70	36.90					
T79	528.77	31.10	11.45	11.26	6.38	8.08	1.78	4.87	0.07	0.47	18.88	27.30	14.9	71.90	160	698	125	10.60	10.50	14.10	55	37.20					
T83	543.18	35.00	11.00	12.80	5.64	4.89	1.82	5.60	0.05	0.54	21.42	9.60	11.1	80.70	211.0	714	166	5.78	3.68	18.20	56	39.00					
T85	552.66	45.05	5.33	16.42	3.54	4.55	2.53	6.80	0.08	0.79	12.65	25.90	18.8	137.00	253.0	417	134	7.15	4.85	10.50	78	42.50					
T86	556.76	23.72	19.25	6.60	10.90	2.88	1.65	2.49	0.13	0.30	29.21	15.40	8.6	53.70	117	1340	131	18.40	26.00	9.20	46	23.70					
T99	594.94	42.29	6.48	14.87	3.92	5.69	2.19	6.54	0.04	0.60	14.01	22.10	13.7	71.50	166	474	77	10.85	2.94	9.80	57	27.90					
T101	603.16	30.65	13.85	10.40	7.70	4.27	1.53	4.78	0.02	0.44	24.49	8.40	9.7	56.80	228	1140	116	3.09	3.80	11.60	45	26.20					
T102	606.1	31.70	13.35	10.88	8.04	3.89	2.54	3.98	0.11	0.53	23.20	19.50	13.6	116.00	156	1320	107	12.10	14.30	12.30	44	28.70					
T109	629.37	30.95	13.20	9.56	8.34	4.37	1.87	4.21	0.04	0.42	21.24	20.00	10.6	66.30	527.0	2740	123	5.91	14.65	8.50	41	28.90					
T115	647.75	31.61	14.60	10.07	6.07	4.71	1.73	4.58	0.09	0.42	19.97	18.80	12.4	57.60	192	920	118	12.00	18.00	10.00	54	37.40					
T116	652	21.93	18.20	6.10	11.45	4.16	1.53	2.58	0.11	0.25	27.38	18.90	9.9	47.20	272	2270	102	13.70	28.9	8.20	39	29.30					
T117	655.3	18.80	19.55	5.72	13.60	2.57	1.22	2.60	0.02	0.22	32.13	12.40	7.5	35.60	83	1890	109	3.22	13.90	10.20	24	18.60					
T123	682.93	33.65	10.80	11.59	7.61	5.66	2.68	4.14	0.02	0.54	18.26	18.10	13.5	119.00	228	1180	133	4.73	11.30	10.70	51	37.30					
T127	696.93	32.27	12.55	9.91	8.44	4.77	3.47	3.14	0.02	0.41	19.26	20.60	11.5	132.50	706.0	1540	119	8.60	9.5	8.60	43	30.10					
T128	700.37	36.31	10.60	10.68	7.89	4.33	2.87	3.26	0.04	0.55	20.09	23.10	13.3	137.00	224.0	1090	96	3.46	27.60	7.30	62	34.30					
T133	719.2	26.06	15.88	8.04	10.40	4.19	2.33	2.80	0.29	0.39	24.06	22.90	12.4	70.90	101.0	1290	131	18.60	73.90	9.60	42	35.00					
T134	720.78	28.20	14.45	8.89	8.12	4.70	2.10	3.58	0.11	0.39	24.54	17.40	12.2	63.30	156	910	105	16.85	27.00	10.10	41	33.90					
T141	746.95	22.86	16.90	7.06	11.60	3.22	2.85	2.07	0.05	0.28	27.35	14.30	8.9	81.00	152	1730	111	3.67	16.65	8.80	53	29.30					
T146	764.56	29.34	13.90	8.41	10.20	4.09	1.34	4.10	0.02	0.36	22.12	18.30	9.8	56.80	165	1230	72	2.24	6.34	6.80	42	27.50					
T154	791.22	28.66	12.55	8.69	8.11	4.19	2.72	3.16	0.09	0.33	25.95	21.60	9.3	45.30	223.0	1180	82	5.86	12.10	6.00	40	31.50					
T156	800.6	24.65	15.75	6.77	10.80	3.56	1.27	3.14	0.04	0.28	28.78	17.90	8.9	52.80	172.5	1090	93	3.36	7.0	7.80	37	22.30					
NO	La	Ce	Pr	Nd	Sm	Eu	Gd	Tb	Dy	Ho	Er	Tm	Yb	Lu	ΣREE	δEu	δCe	Dy/Sm	LREE/HREE	Sr/Ba	CIA	Sr/Cu	Rb/Sr	V/Ni	Ni+V	Ceanom	U/T
T41	34.8	72.7	7.14	25.9	4.85	0.93	4.14	0.61	3.60	0.70	1.87	0.26	1.66	0.27	159.43	0.62	1.05	0.74	11.16	1.73	54.52	14.16	0.19	4.01	0.80	0.0041	0.82
T44	38.2	76.1	7.83	28.0	5.06	0.93	4.04	0.62	3.44	0.72	2.13	0.30	1.88	0.28	169.53	0.61	1.01	0.68	11.64	2.82	54.33	22.02	0.14	6.67	0.87	-0.0062	1.26
T52	31.8	65.7	6.60	23.8	4.32	0.87	3.76	0.54	3.16	0.61	1.79	0.23	1.44	0.23	144.85	0.65	1.04	0.73	11.32	3.55	54.19	33.58	0.09	6.99	0.87	-0.0269	1.33

Table 1 (continued)

NO	La	Ce	Pr	Nd	Sm	Eu	Gd	Tb	Dy	Ho	Er	Tm	Yb	Lu	Σ REE	δ Eu	δ Ce	Dy/Sm	LREE/ HREE	Sr/Ba	CIA	Sr/Cu	Rb/Sr	V/Ni	V/ Ni+V	Ceanom	U/T
T55	29.5	56.6	5.90	21.7	4.09	0.77	3.61	0.57	3.29	0.73	2.13	0.32	2.24	0.35	131.80	0.60	0.98	0.80	8.95	7.09	53.76	36.64	0.09	7.56	0.88	-0.0576	5.89
T58	37.9	76.0	7.88	28.3	5.22	1.04	4.56	0.64	3.62	0.68	1.77	0.26	1.62	0.23	169.72	0.64	1.01	0.69	11.68	1.95	52.32	12.71	0.22	5.50	0.85	-0.0129	0.77
T59	45.8	87.6	9.22	32.9	6.15	1.10	4.78	0.68	3.89	0.73	1.99	0.28	1.69	0.26	197.07	0.60	0.97	0.63	12.78	1.48	59.27	12.21	0.25	4.24	0.81	-0.0100	0.36
T60	19.0	37.0	3.98	14.2	2.65	0.54	2.31	0.32	2.12	0.44	1.42	0.23	1.83	0.32	86.36	0.65	0.98	0.80	8.61	10.82	52.86	62.32	0.06	7.43	0.88	-0.1001	7.53
T61	42.3	84.6	8.57	30.8	5.60	1.05	4.84	0.67	3.84	0.73	1.89	0.27	1.60	0.25	187.01	0.60	1.01	0.69	12.27	2.62	52.44	17.85	0.17	6.37	0.86	0.0087	0.66
T66	44.5	88.6	8.84	30.6	5.36	1.00	4.46	0.61	3.30	0.63	1.75	0.24	1.42	0.21	191.52	0.61	1.02	0.62	14.18	2.21	53.57	13.52	0.24	5.22	0.84	0.0187	0.72
T70	31.2	63.4	6.71	24.5	4.59	0.92	3.77	0.55	3.00	0.61	1.62	0.22	1.50	0.23	142.82	0.66	1.01	0.65	11.42	1.98	53.83	14.25	0.26	6.82	0.87	0.0037	0.73
T79	31.9	69.0	7.28	28.6	5.21	1.06	4.72	0.68	4.00	0.73	1.96	0.27	1.66	0.25	157.32	0.64	1.05	0.77	10.02	4.38	49.43	18.76	0.10	4.58	0.82	0.0074	0.99
T83	34.3	70.6	6.98	26.1	5.84	1.11	5.26	0.70	3.80	0.72	1.81	0.25	1.55	0.23	159.25	0.60	1.04	0.65	10.12	3.38	49.57	18.31	0.11	17.29	0.95	0.0005	0.64
T85	48.7	91.5	8.92	30.1	5.41	0.88	3.83	0.46	2.41	0.44	1.17	0.17	1.05	0.16	195.20	0.56	0.98	0.45	19.14	1.65	53.29	9.81	0.33	5.17	0.84	-0.0005	0.68
T86	19.6	41.4	4.64	17.7	3.74	0.67	3.35	0.48	2.86	0.57	1.63	0.25	1.58	0.25	98.72	0.57	1.01	0.76	8.00	11.45	49.89	56.54	0.04	8.51	0.89	-0.0953	1.41
T99	69.9	135.3	14.00	47.9	6.85	1.01	3.75	0.43	2.01	0.39	1.01	0.15	0.95	0.15	283.80	0.55	0.98	0.29	31.10	2.86	49.65	16.99	0.15	3.48	0.78	0.0184	0.27
T101	26.1	51.4	5.56	18.6	3.24	0.55	2.41	0.38	1.96	0.39	0.99	0.15	0.99	0.17	112.89	0.58	0.98	0.60	14.17	5.00	48.39	43.51	0.05	13.81	0.93	-0.0349	1.23
T102	29.4	58.2	6.11	22.3	4.49	0.79	3.95	0.58	3.24	0.59	1.62	0.22	1.34	0.20	133.03	0.56	0.99	0.72	10.33	8.49	50.89	45.99	0.09	5.49	0.85	-0.0039	1.18
T109	53.2	88.5	8.49	24.1	3.43	0.56	2.35	0.33	2.11	0.39	1.17	0.16	1.16	0.18	186.13	0.57	0.91	0.62	22.71	5.20	48.16	94.81	0.02	6.15	0.86	-0.0301	2.48
T115	24.0	52.2	5.95	22.1	4.64	0.86	4.00	0.57	3.13	0.62	1.64	0.23	1.46	0.23	121.63	0.60	1.02	0.67	9.24	4.80	48.04	24.60	0.06	6.28	0.86	-0.0410	1.50
T116	21.5	45.4	5.07	18.2	3.67	0.73	3.00	0.46	2.70	0.57	1.52	0.23	1.43	0.20	104.68	0.65	1.01	0.74	9.35	8.35	47.69	77.47	0.02	5.40	0.84	-0.0985	2.11
T117	13.0	27.3	2.67	9.2	1.61	0.28	1.48	0.23	1.30	0.28	0.88	0.13	0.83	0.13	59.32	0.55	1.06	0.81	10.28	22.66	47.12	101.61	0.02	8.79	0.90	-0.0444	4.32
T123	25.6	50.5	5.30	18.1	3.71	0.72	3.14	0.44	2.51	0.48	1.34	0.19	1.21	0.19	113.43	0.63	0.99	0.68	10.94	5.18	51.40	31.64	0.10	7.35	0.88	-0.0866	2.39
T127	40.1	77.5	7.85	25.4	4.37	0.77	3.10	0.48	2.58	0.51	1.48	0.19	1.18	0.16	165.67	0.61	0.99	0.59	16.11	2.18	50.41	51.16	0.09	5.78	0.85	-0.0029	1.10
T128	15.6	30.8	3.17	10.8	2.06	0.43	1.65	0.27	1.73	0.35	0.90	0.13	0.88	0.13	68.90	0.69	1.00	0.84	10.41	4.87	53.21	31.78	0.13	4.16	0.81	-0.1386	7.98
T133	28.6	59.7	6.57	23.5	4.29	0.97	4.03	0.59	3.37	0.63	1.79	0.27	1.55	0.22	136.08	0.70	1.01	0.79	9.93	12.77	50.34	36.86	0.05	5.72	0.85	0.0409	3.97
T134	23.0	50.3	5.70	21.0	4.28	0.84	3.69	0.53	2.99	0.58	1.51	0.21	1.31	0.20	116.14	0.63	1.03	0.70	9.54	5.83	48.98	26.84	0.07	6.03	0.86	0.0370	1.60
T141	12.5	26.1	2.79	9.9	1.89	0.36	1.65	0.24	1.47	0.32	0.90	0.14	0.89	0.14	59.29	0.61	1.02	0.78	9.31	11.42	50.25	59.04	0.05	7.76	0.89	-0.2022	4.54
T146	31.8	62.5	6.60	22.3	3.46	0.68	2.75	0.34	2.03	0.43	1.16	0.17	1.06	0.17	135.45	0.65	0.99	0.59	15.70	7.48	46.85	44.73	0.05	3.93	0.80	-0.0884	2.83
T154	21.9	44.1	4.55	17.1	3.14	0.61	2.54	0.36	2.03	0.39	1.05	0.16	1.09	0.16	99.18	0.64	1.01	0.65	11.75	5.29	49.01	37.46	0.04	3.80	0.79	-0.0326	2.06
T156	19.3	38.9	3.79	13.3	2.21	0.42	1.70	0.25	1.41	0.29	0.84	0.14	1.01	0.16	83.72	0.64	1.03	0.64	13.43	6.32	47.28	48.88	0.05	5.20	0.84	-0.0538	2.09

REE, Trace elements: $\mu\text{g/g}$; Main elements: %, tests completed in ALS Chemex (Guangzhou) Co Ltd; $\delta\text{Eu} = \text{Eu}_N/[(\text{Sm}_N + \text{Gd}_N)/2]$; $\delta\text{Ce} = \text{Ce}_N/[(\text{La}_N + \text{Pr}_N)/2]$

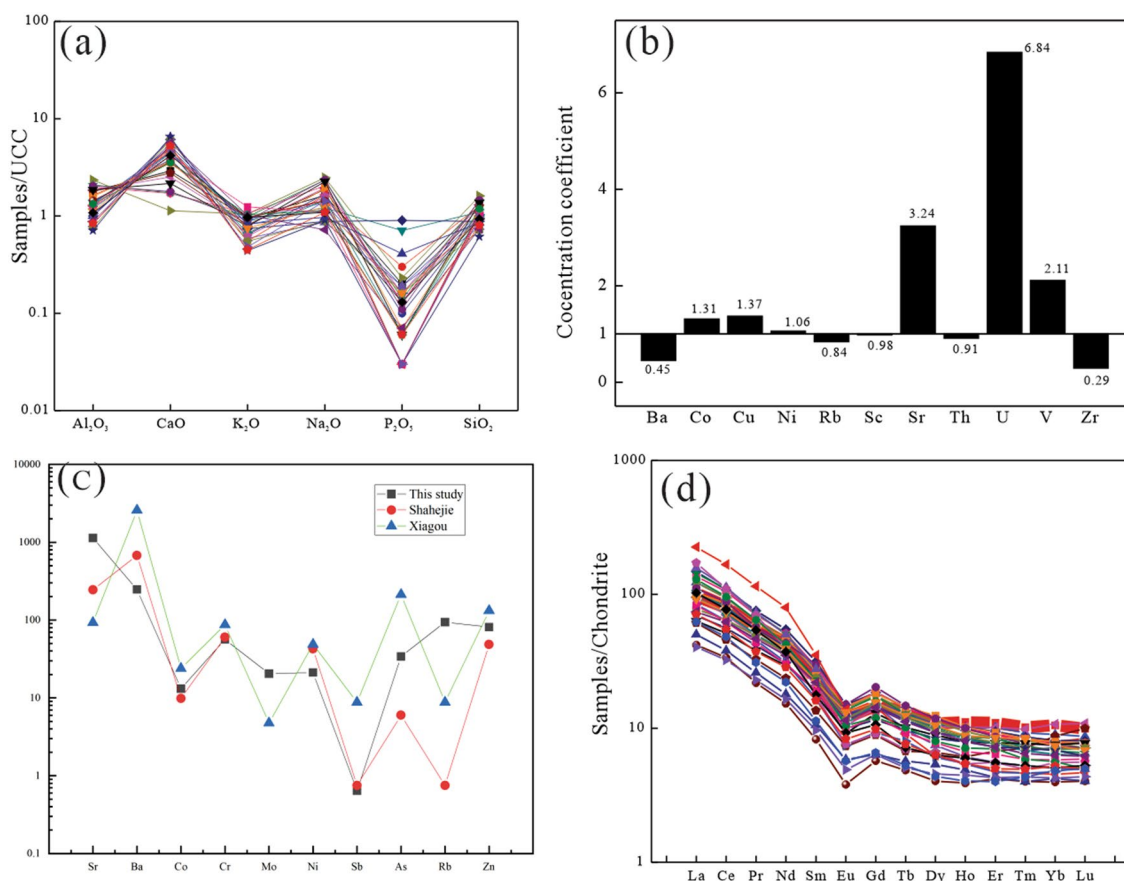


Fig. 4 Geochemical characteristics of the Tamusu Mudstone. **a** abundance characteristics of major elements; **b** abundance characteristics of trace; **c** comparisons of trace element abundances with typical hydrothermal sedimentary rocks; **d** distribution pattern diagram of REEs

Based on the above-mentioned mineral assemblages, typical structures and geochemical characteristics of Tamusu Mudstone, it could be concluded that Tamusu Mudstone belongs to a set of typical lacustrine hydrothermal sedimentary rocks. Moreover, typical hydrothermal structures, geochemical and mineral characteristics of the Tamusu Mudstone, sedimentary environment, and hydrothermal sedimentary model are well discussed.

5 Discussions

5.1 Hydrothermal sedimentary structures

Hydrothermal sedimentary rock is formed from the mixing of underground hot water or magmatic hydrothermal with seawater or lake water. According to characteristics of hydrothermal mineral assemblages and geochemistry, hydrothermal sedimentary rock can be divided into two types: "black smoke" and "white smoke" (Brown, 1992). The "black smoke" is featured by large amounts of metal sulfides at high temperatures (> 350 °C). The "white smoke" is featured

by silicate, aluminosilicate and carbonate rocks at low temperatures (32–320 °C) (Scott, 1997; Zheng et al., 2018). Recent findings summarizing "white smoke" hydrothermal sedimentary rocks in an inland lake basin in Northwest China have indicated that the hydrothermal mineral assemblages are mainly composed of dolomite, ankerite, analcime and albite. The structure is dominated by lamellar structures, and typical structural features such as matrix-supported, banded, network and contemporaneous deformation, which are obviously different from burial and microbial origins (Zheng et al., 2018; Chen et al., 2018; Zhong et al., 2018; Zhu et al., 2020). Therefore, the above-mentioned mineral assemblages and typical structures of the Tamusu Mudstone are in accordance with the hydrothermal sedimentary structures.

(1) Dolomite

According to crystal grain-size, Mud-micro, powder-fine and coarse-grained rhombic dolomite could be

Table 2 Comparisons of trace element in the Tamusu hydrothermal-sedimentary rock and other typical areas

Location	No	Ni	Cr	Co	Sb	As	Rb	Zn	Ba	Sr
This study	T41	33.40	70	19.7	1.03	15.8	122.0	114	375	650
	T44	26.40	60	17.6	1.15	25.2	129.5	120	337	949
	T52	22.60	60	14.4	0.67	9.8	103.0	83	325	1155
	T55	26.60	60	14.2	0.84	20.6	122.0	89	187.5	1330
	T58	27.80	70	18.5	0.62	9.5	119.5	103	276	539
	T59	37.50	100	20.9	0.29	12.1	171.0	94	458	679
	T60	18.70	40	11.7	1.35	16.8	98.3	80	159.0	1720
	T61	24.50	70	15.7	0.38	11.6	122.5	95	282	739
	T66	27.00	80	18.0	1.18	7.2	145.0	104	269	595
	T70	19.20	70	12.6	0.41	5.3	136.5	88	265	526
	T79	27.30	60	14.9	0.95	10.0	71.9	59	159.5	698
	T83	9.60	73	11.1	0.19	2.4	80.7	84	211	714
	T85	25.90	80	18.8	1.11	6.7	137.0	117	253	417
	T86	15.40	40	8.6	0.31	45.2	53.7	61	117.0	1340
	T99	22.10	42	13.7	0.36	81.8	71.5	85	166.0	474
	T101	8.40	79	9.7	0.28	8.1	56.8	123	228	1140
	T102	19.50	49	13.6	0.35	12.0	116.0	91	155.5	1320
	T109	20.00	49	10.6	0.58	54.2	66.3	62	527	2740
	T115	18.80	71	12.4	0.45	41.4	57.6	87	191.5	920
	T116	18.90	41	9.9	0.33	65.9	47.2	54	272	2270
	T117	12.40	34	7.5	0.20	27.2	35.6	51	83.4	1890
	T123	18.10	59	13.5	0.81	65.7	119.0	67	228	1180
	T127	20.60	50	11.5	0.46	25.0	132.5	85	706	1540
	T128	23.10	51	13.3	1.07	113.0	137.0	70	224	1090
	T133	22.90	40	12.4	1.25	68.0	70.9	56	101.0	1290
	T134	17.40	51	12.2	0.41	67.3	63.3	65	156.0	910
	T141	14.30	40	8.9	0.27	44.1	81.0	63	151.5	1730
	T146	18.30	32	9.8	1.17	94.3	56.8	75	164.5	1230
	T154	21.60	41	9.3	0.48	36.6	45.3	50	223	1180
	Mean	21.21	56.43	13.13	0.64	34.00	94.07	81.17	247.46	1134.83
Shahejie Formation (Dai et al., 2008)		128	91	9.7	0.8	6.7	114	38	735	58
		24	77	16.5	1.1	10.5	95	45	775	88
		6	42	7.8	0.6	3.1	56	50	554	64
		13	31	5.5	0.5	3.7	29	61	644	769
	Mean	42.75	60.25	9.88	0.75	6	73.5	48.5	677	244.75
Xiagou Formation (Zheng, et al., 2018)	Mean	48.8	87	23.9	8.76	212.9	97.3	131.9	2581	92.9

determined in the Tamusu sedimentary rocks. Mud-micro dolomite has a strip-like interbedded structure with analcime and argillaceous minerals (Fig. 5a, b). Powder-fine dolomite that is distributed in a network structure is semi-self-shaped, with grain sizes varying from 50 μm to 500 μm (Fig. 3d; Fig. 5c). The morphological differences in crystals indicate that mud-micro dolomite recrystallization to powder-fine dolomite could be excluded. Coarse-grained rhombic dolomite can

be identified as having a matrix-supported structure, and the grain sizes are up to 0.5 mm and 1 mm (Fig. 3d, f).

Dolomites with saddle-like and zebra-like structures have been proven to be products of hydrothermal metasomatism in marine hydrothermal dolomites (Davies & Smith, 2006; Feng et al., 2017; Liu et al., 2017; Koeshidayatullah et al., 2020). Dolomite with a microbial origin usually forms unique microstructures (mucosal, nanoparticle, fibrous network, radial and

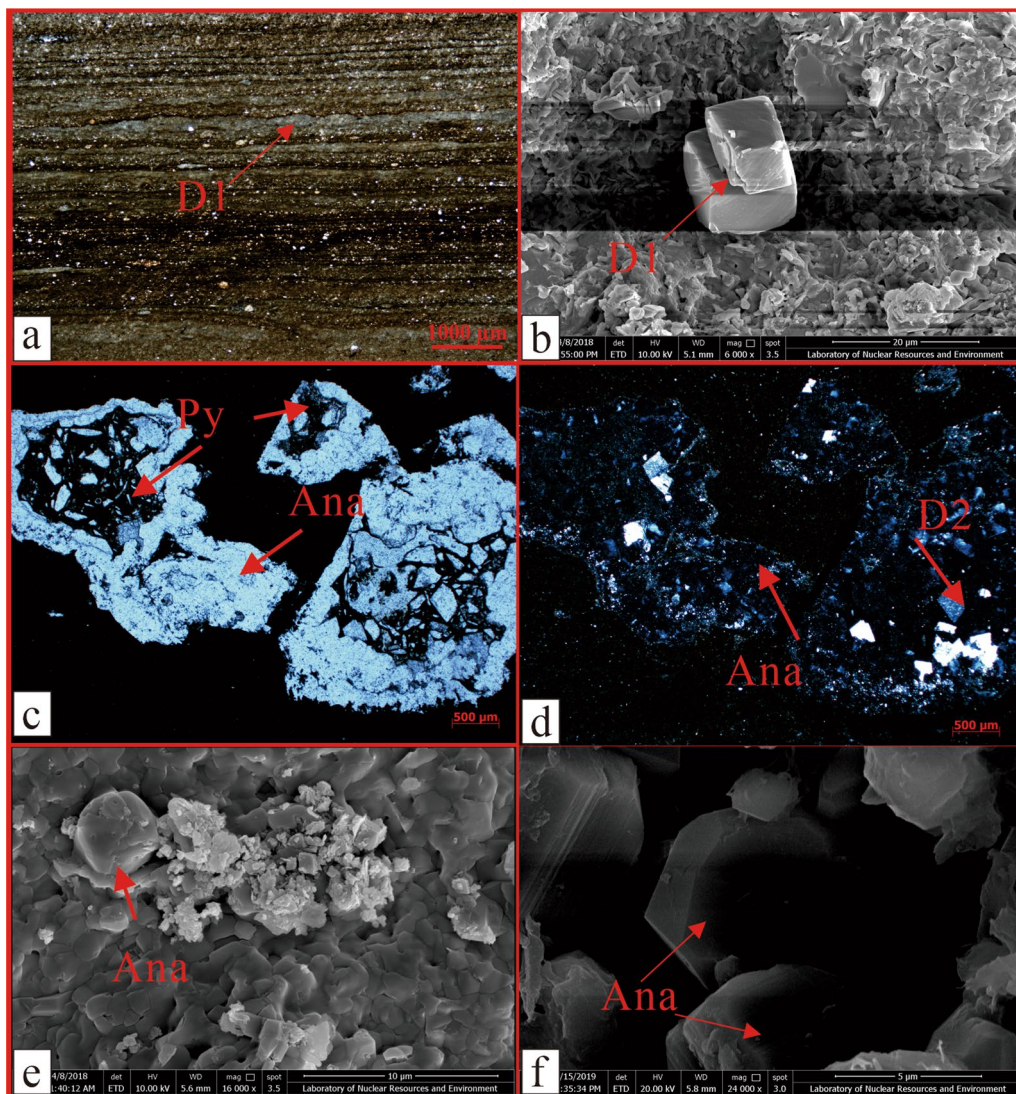


Fig. 5 Typical minerals characteristics of host rock in the Tamusu pre-selected area **a** Mixed laminae of mud-micro dolomite, analcime and argillaceous, Borehole TZK-2, 313.25 m, single polarization light; **b** mud-micro dolomite observed by SEM, Borehole TZK-2, 2752m; **c** field of views same as **d** analcime with first-order grey interference colors and, filling with dolomite. Analcime is mixed and distributed within the dark clay material, crossed polarization light, Borehole TZK-2, 638 m; **e** analcime crystals are dissolved into irregular tetragonal trisoctahedron, TZK-1, 593.53m; **f** typical tetragonal trisoctahedron analcime is observed by SEM, Borehole TZK-2, 530 m; D1: mud-micro dolomite; D2: powder-fine dolomite; Ana: analcime; Ank: ankerite; Py: Pyrite

cluster structure, etc. (Bontognali et al., 2012; Zhai et al., 2017). Coarse-grained rhombic dolomite in the Tamusu Mudstone may be formed by hydrothermal deposits processes. The hydrothermal fluids may have generated vibration when the pressure in the environment changed from high-pressure to low-pressure, resulting in the rhombic structure of dolomite clasts. In addition, the flocculation of various chemical components is due to charged ions when the underground hydrothermal solution is mixed with cold lake water (Zhong et al., 2018). The coarse-grained rhombic dolomites are

characterized by high Mg/Ca ratios (0.494–0.607, avg. 0.56) (Table 3), showing similar ratios to those of typical lacustrine hydrothermal areas, such as the Pingdiquan Formation in eastern Junggar (Li et al., 2017; Wen et al., 2014).

(B) Analcime

Analcime belongs to the zeolite group, and is a tectosilicate with the chemical formula $\text{NaAlSi}_2\text{O}_6 \cdot \text{H}_2\text{O}$, where Na could be replaced by small amounts of K^+ and

Table 3 EPMA analysis of analcime and dolomite in Tamusu hydrothermal-sedimentary rock

Minerals	Borehole	Depth/m	Test points	K ₂ O	Al ₂ O ₃	SiO ₂	FeO	CaO	Na ₂ O	MgO	Total
Analcime	ZHK88-15	240	18-001-s1	0.035	21.321	61.479	0.084	0.225	9.014	0.131	92.295
			18-001-s2	0.044	21.802	60.209	0.115	0.249	6.424	0.088	88.931
			18-001-s3	0.069	21.138	57.698	0.037	0.113	12.986	0.031	92.072
			18-001-s4	0.072	20.257	59.085	0.089	0.271	11.938	0.045	91.767
			18-001-s5	0.193	20.224	60.065	0.672	0.067	10.877	0.162	92.306
			18-001-s6	0.013	20.383	57.487	0.052	0.218	12.265	0.03	90.467
	TZK-2	686	T124-s1	0.061	19.988	60.377	0.115	0.078	12.161	0.043	92.853
			T124-s2	0.329	20.741	61.255	0.182	0.469	8.592	0.244	91.812
			T124-s3	0.041	20.267	59.349	0.074	0.018	12.297	0.013	92.094
			T124-s4	0.238	19.87	59.339	0.165	0.433	11.918	0.265	92.234
	ZKH104-8	224	T124-s5	0.029	19.834	60.346	0.067	0.031	12.075	0.011	92.393
			18-016-s1	0.012	19.77	64.781	0.006	0.097	8.269	0.01	92.989
			18-016-s2	0.027	20.8	63.982	0.043	0.181	8.402	0.045	93.484
			18-016-s3	0.265	19.494	65.843	0.112	0.264	7.374	0.133	93.577
	TZK-2	493	18-018-s1	0.024	20.854	61.991	0.072	0.266	10.911	0.004	94.122
			18-018-s2	0.025	20.101	61.998	0.107	0.251	10.004	0.104	92.59
			18-018-s3	0.011	20.329	61.034	0.052	0.736	11.019	0.023	93.204
	TZK-1	523	523-s5	0.027	19.951	62.046	–	0.065	10.694	–	92.783
	TZK-2	538	18-021-s2	0.029	20.538	62.235	0.038	0.152	11.163	0.052	94.207
	TZK-2	523	18-019-s2	0.021	20.619	63.112	0.099	0.698	8.129	0.517	93.204
	ZHK88-15	240	18-001-s11	0.021	0.077	0.144	0.162	29.673	0.202	20.144	50.548
			18-001-s12	0.103	0.239	0.86	0.663	29.266	0.182	19.324	50.729
Dolomite	TZK-1	523	593-s5	0.183	0.295	0.926	0.569	29.256	0.214	20.83	52.695
			523-s1	0.064	0.131	6.55	0.29	28.731	0.137	18.824	54.908
			523-s2	0.091	0.242	0.537	0.27	33.036	0.162	19.413	53.813
			523-s3	0.149	0.388	0.947	0.367	30.092	0.127	20.552	52.834
	TZK-2	715	T132s	0.198	0.259	0.959	0.186	29.273	0.263	21.15	52.429
		686	T124-s8	0.105	0.36	0.873	1.216	28.888	0.223	19.296	50.986
		538	18-021-s1	0.171	0.877	2.427	1.465	29.284	0.302	18.675	53.513

EPMA tests completed in ECUT by JXA-8230

Ca²⁺. Analcime can be identified as the intercalation of dolomite and argillaceous layers. The irregular tetragonal trisoctahedron crystals have a matrix-supported structure. Analcime exhibits first-order grey interference colors, filling with dolomite (Fig. 5c, d). Moreover, typical and dissolved tetrahedral trisoctahedron are observed by SEM (Fig. 5e, f). Detailed observations failed to determine low-grade metamorphic minerals such as laumontite and prehnite, indicating that the genesis of metamorphic or primary analcime could be ruled out. The Si/Al ratios of analcime are characterized by high silica (2.316–2.866, avg. 2.545) (Table 3), which is obviously higher than the sedimentary diagenetic type of analcime formed by sedimentary diagenesis

and low-grade metamorphism, and higher than that of low silicon analcime that is directly crystallized from highly alkaline water. This type has Si/Al ratios that are closer to those of high silicon analcime, which is commonly affected by siliceous volcanic glass and alkaline hydrothermal solution. Above-mentioned mineral assemblages generally show that hydrothermal fluid is mainly a medium–low temperature "white smoke" hydrothermal fluid that is rich in CO₃²⁻, Na⁺, Al³⁺, Si⁴⁺, Mg²⁺, Fe²⁺ and Ca²⁺ and relatively poor in metal sulfides (Zheng et al., 2018; Zhong et al., 2018). As a result, analcime may have formed by the direct crystallization of alkaline hydrothermal fluids mixed with lake water when

alkaline hydrothermal fluids containing Na^+ , Ca^{2+} and CO_3^{2-} vented out of lake bottom.

5.2 Sedimentary environment

(1) Palaeoclimate

The calculated chemical index of alteration (CIA) values vary between 46.85 and 59.27, with an average of 51.03, and the Sr/Cu values are greater than 5, confirming a relatively dry sedimentary environment (Xiang et al., 2019). The dry–wet transitions of palaeoclimate at depths of approximately 450 m and 550 m are also determined by the vertical evolutions of the two indicators. Meanwhile, the calculated CIA values indicate that the samples with low weathering are not affected by proximal clastic deposition. A negative correlation was observed between the vertical trend of Sr/Cu values and that of Rb/Sr values, further confirming that mudstone underwent dry–wet transitions.

(B) Palaeo-salinity

The Sr/Ba values are all greater than 1 (avg. 5.86), indicating a saline environment (Campbell & Williams, 1965). The vertical trend of Sr/Ba values is mostly synchronous with that of Sr/Cu values, which indicates that the salinity increases correspondingly as dryness increase. That is, the response of paleo-salinity change to dry–wet transitional features was also showed at the same depths in the target Bayingebi Formation.

(C) Redox

The V/Ni and V/(V + Ni) values in Table 4 show a high correlation, indicating that the mudstone is under an anaerobic and a strongly reducing environments. Slight fluctuations occurred in anaerobic and reducing environment, which may have been the response of the abnormally dry climate at that time. Vertically,

the redox environment correlates very well with the palaeoclimate change.

The correlations between δCe and δEu , δCe and (Dy/Sm) failed to reach significant levels, indicating that the samples were not affected by diagenesis or were affected by weak diagenesis. Therefore, the REE data was used to discuss the depositional environment. The U/Th and normalized Ce values confirm the existence of a temporary oxidizing sedimentary environment under anaerobic and strongly reducing conditions. Among the 30 samples, 7 samples with $\text{U/Th} < 0.75$ and 3 samples with $\text{Ce}_{\text{anom}} < -0.1$ confirm the existence of an oxidizing environment, and the depths of interfaces are highly coupled with the depths-changes in palaeoclimate and palaeo-salinity mentioned above.

The low-temperature "white smoke" hydrothermal sedimentary rocks are formed in arid, anaerobic and strongly reducing saline lake environments. Meanwhile, the consistent pyrite contents indicate a strongly reducing environment. Vertically, palaeoclimate fluctuations are synchronous with changes in the main mineral contents and typical sedimentary structures (Fig. 6). Those fluctuation interfaces are correlated; however, their internal connections and mutual influence need to be further explored.

5.3 Hydrothermal sedimentary model

It is worth noting that the Altun fault at 100–120 Ma has experienced multi-stage activities (Li et al., 2006; Wu et al., 2010) and several typical lacustrine hydrothermal sedimentary rocks have been reported along the fault in recent years (Zhu et al., 2020). Examples include the Lower Cretaceous Xiagou Formation mudstone in the Jiuxi Basin (Zheng et al., 2018; Wen et al., 2014); the Lower Cretaceous Suhongtu Formation and Bayingebi Formation mudstone in the Hari Sag, Yiner Basin (Chen et al., 2018); and the Lower Cretaceous Tengger Formation mudstone in the Baiyinchagan Sag, Erlian Basin (Zhong et al., 2018). These typical hydrothermal sedimentary rocks mostly formed in the Early Cretaceous. The typical hydrothermal sedimentary areas

Table 4 Redox environment indexes for mudstone

Indexes	Data range/avg	Redox			References
		Anaerobic	Poor oxygen	Oxidizing	
V/Ni	3.8–17.29/6.52	> 1		< 1	Jones and Manning (1994)
V/(Ni + V)	0.78–0.95/0.85	> 0.6	0.46–0.6	< 0.46	Jones and Manning (1994)
U/Th	0.27–7.98/2.18	> 1.25	0.75–1.25	< 0.75	Jones and Manning (1994)
Ce_{anom}	–0.2022– 0.0409/–0.03431.0062	> –0.1		< –0.1	Elderfield and Greaves (1982)

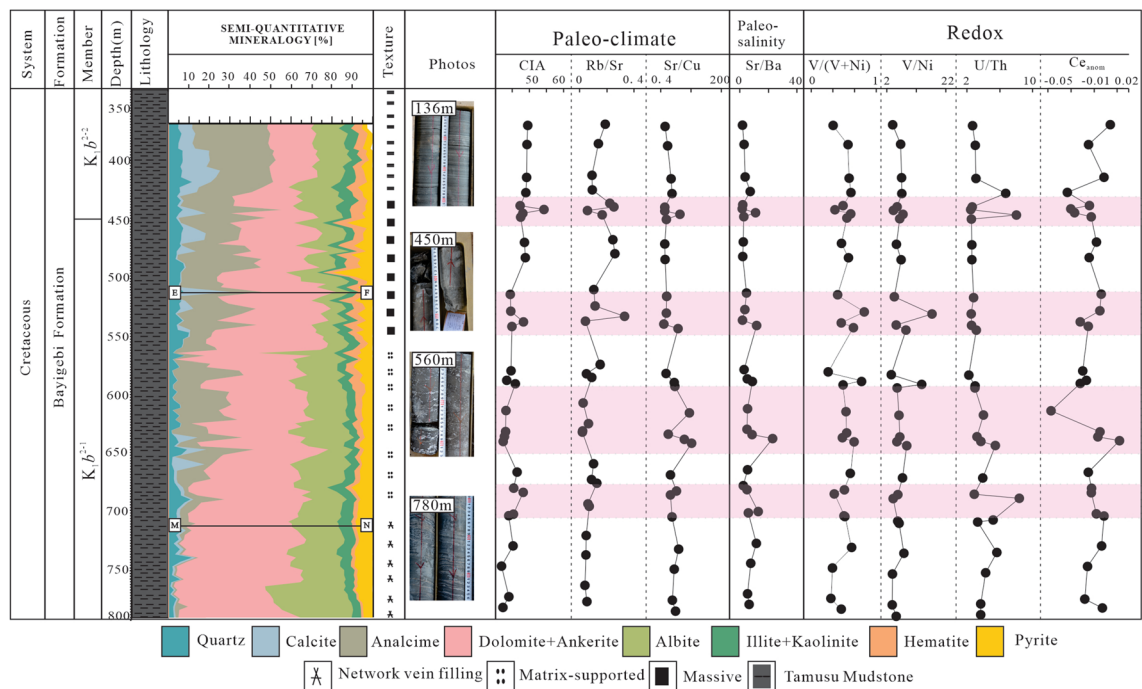


Fig. 6 Vertical variations of geochemical parameters and mineral compositions of the Tamusu Mudstones

in different basins that formed in the Early Cretaceous are located within a distance of nearly 1000 km. Therefore, the Late Cretaceous tectonic activities in the Altun fault may have been the main factor controlling the formation of these typical hydrothermal sedimentary rocks. Controlled by multi-periods activities of the Altun fault, interactions between volcanic eruptions (magmatic activity) and sub-lacustrine hydrothermal fluids have resulted in a set of typical low-temperature "white smoke" hydrothermal sedimentary rocks.

In the Early Cretaceous stage, the Bayingebi Basin was in a comprehensive pull-out stage that was controlled by the Altun fault. Under the action of gravity and overlying pressure, the lake water seeped down along the main faults and underwent water-rock reactions for a long time. The process extracted ions including Na^+ , Al^{3+} , Si^{4+} , Mg^{2+} , Fe^{2+} , and Ca^{2+} from the surrounding rock to form hot brine in the magma chamber. Then, driven by thermal energy, fluid potential energy and the heat gradient, the hot brine was discharged into the lake basin. The introduction of Mg^{2+} and the removal of Ca^{2+} are a key process in the formation of dolomite during the water-rock reactions, which provides the enough Mg^{2+} -rich fluids. The reaction is $2\text{CaCO}_3 + \text{Mg}^{2+} = \text{CaMg}(\text{CO}_3)_2 + \text{Ca}^{2+}$ (Wang, 2014); Moreover, Na^+ -rich fluids provided by the water-rock reactions play an important role in formation of analcime, and the reaction can be written as:

$\text{KAlSi}_3\text{O}_8 + \text{Na}^+ + \text{H}_2\text{O} = \text{NaAlSi}_2\text{O}_6 \cdot \text{H}_2\text{O} + \text{K}^+ + \text{SiO}_2$; With proper temperature, analcime is transformed into albite, and the reaction can be written as: $\text{NaAlSi}_2\text{O}_6 \cdot \text{H}_2\text{O} + \text{SiO}_2 = \text{NaAlSi}_3\text{O}_8 \cdot \text{H}_2\text{O}$ (Zhu et al., 2012; Shi et al., 2021). Therefore, a certain amount of albite is determined by the XRD analysis mentioned above. This continuous circulation of lake water infiltration and hydrothermal upwelling convection provided a heat source and mineralization ions for the lake basin.

When upwelling hydrothermal fluid migrates to the volcanic eruption vent, the difference in the crystallization differentiation of hydrothermal minerals and the formation of typical mineral assemblages were controlled by the difference in physical and chemical conditions due to the distance to the vent. As a result, typical minerals such as dolomite and analcime, formed, and their assemblages contribute to the laminar, mud-supported and other typical structures described above (Fig. 7).

5.4 Suitability for HLW disposal considerations

The set of low-temperature "white smoke" hydrothermal sedimentary rocks in the Tamusu pre-selected are contributes to the higher contents of main minerals such as dolomite and analcime, which are distinct from COX and OPA clays. Shale classification ternary diagrams (Zhong et al., 2018) were used to compare the Tamusu

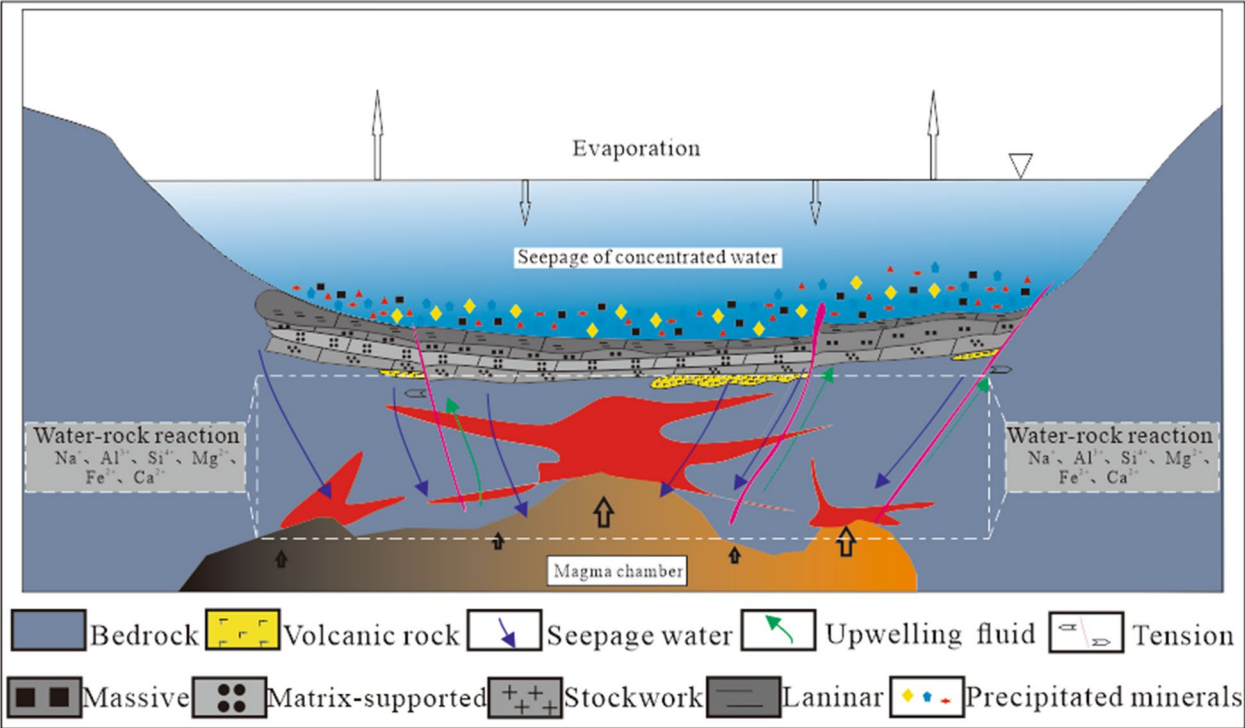


Fig. 7 Sedimentary model of lacustrine hydrothermal rock of the Tamusu Mudstone

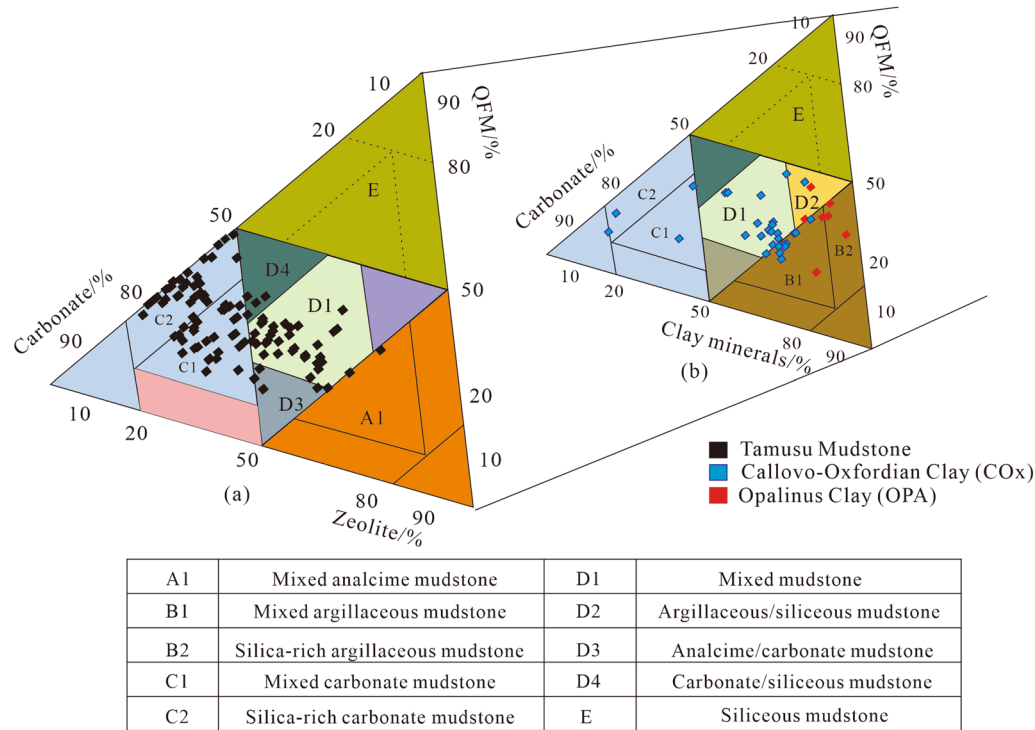


Fig. 8 Classification triangle diagram of the Tamusu Mudstone, COX clay and OPA clay based on Zhong et al. (2018). **a** Tamusu data points; **b** COX and OPA data points. The COX clay data are from Gaucher et al. (2004) and the OPA clay data are from Ould Bouya (2014) QFM=quartz + feldspar + mica

Mudstone with COX and OPA clays. The COX clay and the Tamusu Mudstone are mainly characterized as mixed mudstones (Area D1, Fig. 8), with the clay mineral content being generally higher in OPA clay. The carbonate minerals of the Tamusu Mudstone are dominated by dolomite and ankerite, whereas calcite dominates in COX and OPA clays. Overall, the Tamusu Mudstone, which is mainly dominated by analcime and dolomite, in contrast to the COX and OPA clays, is a new type of argillaceous host rock. The analcime may play a role with respect to radionuclide retention, as discussed in the case of the potential Yucca Mountain host rock (Bish, 1999) and for low- and intermediate-level short-lived radioactive waste in Belgium (Misaelides, 2019). In view of functions of analcime channels and molecular sieves, mudstones bearing analcime have advantages over typical clay rocks (host rocks) in terms of radionuclide adsorption, water content, thermal stability and permeability (Wang et al., 2022; Yu et al., 2021). The primary pores of mudstone filled with dolomite and analcime cement also highlight the advantages of the uniaxial compressive strength of mudstone, which contribute to engineering construction more than typical clay rocks (Wang et al., 2018c). Moreover, the comparison of some physical and mechanical properties between the Tamusu Mudstone and foreign clay rocks are listed in Table 5, showing that in terms of continuous thickness, water content, porosity, and uniaxial compressive strength, the Tamusu Mudstone also has the advantage of being a potential host rock for a disposal repository purposes.

Based on geophysical and crustal structure characteristics in the Tamusu area and from the

neotectonic movement of adjacent areas, the Tamusu area is characterized by peneplain landforms and a relatively stable tectonic environment (Gao et al., 2013). The fault activities in the Tamusu area mainly occurred in the Cretaceous and before the Cretaceous, and the Quaternary strata has not been dislocated by faults, indicating that there has been almost no obvious fault activity since the Quaternary (Rao et al., 2021). Detailed research on the Tamusu Fault (Fig. 1A) indicates that the fault has been in a stable state since (56.8 ± 5.2) ka (Rao, et al., 2020). According to the classification standards of China earthquake intensity scale of I~XII, the seismic intensity in Tamusu area is all classified below VI, and no earthquake with an M_s greater than 5 has ever occurred in that area (Du et al., 2017). Therefore, the preliminary investigations of tectonic activities have confirmed that the Tamusu area has been in a stable stage and that the previous hydrothermal activity in the Bayingebi Basin contributed to the Tamusu Mudstone that is characterized by analcime and dolomite. Certainly, intensive investigations and long-term stability monitoring should be carried out in the Tamusu pre-prelected area. Additionally, the advantages and disadvantages of the Tamusu Mudstone compared to other potential host rocks remain to be assessed carefully in the future.

6 Conclusions

The petrological and geochemical characteristics contribute to the understanding of the hydrothermal sedimentary genesis of the Tamusu Mudstone. The main conclusions are as follows:

Table 5 Comparison of physical and mechanical properties between the Tamusu Mudstone and foreign clay rocks

Parameters	Country			
	France (COX Clay)	Switzerland (OPA Clay)	Belgium (Boom Clay)	China (Tamusu Mudstone)
Continuous thickness (m)	130	131	100	>400
Water content (%)	2.8–8.7/6.7	5–8.9/6.6	28	0.74–9.97/5.45
Porosity (%)	9–18/14	14–25/17	54 (<2 μm)	13–25
Permeability coefficient (m/s)	10^{-14} – 10^{-12}	10^{-14} – 10^{-12}	2×10^{-12} – 4×10^{-12}	10^{-14} – 10^{-12}
Bulk density (g/cm^3)	2.4 ± 0.02	2.4–2.53	2.67	1.94–2.34
Particle density (g/cm^3)	2.7 ± 0.01	2.74–2.79	–	2.61–2.69
Uniaxial compression (Mpa)	12–49	23.1–28.1	2.0–2.2	36–94
Elastic modulus (GPa)	2.3–11	2.1–3.5	–	3.11–12.28
Tensile strength (Mpa)	0.9–5.4	1–2	–	4–16
Poisson's ratio	0.17–0.4/0.3	0.28–0.38	0.4	0.14–0.48
Thermal conductivity ($\text{W} \cdot \text{m}^{-1} \cdot \text{K}^{-1}$)	1.47	1–3.1	Horizontal:2.33 Vertical:1.77	1.12–1.64

Notes: '–' means no data has been collected; The elastic modulus and Poisson's ratio are obtained under uniaxial test conditions. Data collected from: Witherspoon & Bodvarsson, 2001 Distinguin & Lavanchy, 2007; Bernier et al., 2007; Boulila et al., 2008; Yven et al., 2007; Bossar et al., 2017; Wang, 2018b)

(1) Typical structures, mineral assemblages and geochemical characteristics confirm that the host rock has the characteristics of hydrothermal sedimentary rocks, indicating higher contents of dolomite and analcime.

(2) Geochemical analysis concludes that host rock is a low-temperature "white smoke" hydrothermal sedimentary rock that formed in arid, anaerobic and strongly reducing saline lake environment. Vertically, the palaeo-salinity and redox environment were also coupled with the dry–wet evolution, and there was a transient oxidizing environment.

(3) The 100–120 Ma tectonic activity of the Altun fault in the Early Cretaceous, provided the migration pathway for water rock reactions, and may have been the main factor controlling the formation of such mineral assemblages and typical structures.

The discovery of this set of hydrothermal sedimentary rocks not only provides another typical example for studying hydrothermal sedimentary rocks but also has important practical significance to conduct suitability evaluations on Tamusu Mudstone for China's argillaceous-based site screening purposes.

Acknowledgements

The authors are very grateful to the Geological Team No. 208, CNNC, for their support and assistance during the field visit and data collection.

Author contributions

All authors have contributed significantly, and all authors are in agreement with the content of the manuscript. All authors read and approved the final manuscript.

Funding

This manuscript is financially supported by the State Key Laboratory of Nuclear Resources and Environment, East China University of Technology (2020NRE15; 2022NRE-LH-01), Key Laboratory for Digital Land and Resources of Jiangxi Province, East China University of Technology (DLLJ202210), Doctoral Program of East China University of Technology (DHBK2020017) and the Second Division of Science and Technology, China National Defense Science and Technology Bureau (2014)1587.

Availability of data and materials

All data generated or analyzed during this study are included in this published article.

Declarations

Ethics approval and consent to participate

Not applicable.

Consent for publication

The authors declare that the paper is being submitted for consideration for publication in Swiss Journal of Geosciences and that the content has not been published or submitted for publication elsewhere, in any language.

Competing interests

The authors declare no competing interests.

Received: 17 November 2022 Accepted: 27 March 2023

Published online: 24 May 2023

References

- Bernier, F., Li, X. L., & Bastiaens, W. (2007). Twenty-five years' geotechnical observation and testing in the Tertiary Boom Clay formation. *Géotechnique*, 57(2), 229–237.
- Bish, D.L. (1999). Natural Zeolites and Nuclear-Waste Management: The Case of Yucca Mountain, Nevada, USA. In: Natural Microporous Materials in Environmental Technology (pp. 177–191). Dordrecht, Springer Netherlands
- Bontognali, T., Vasconcelos, C., Warthmann, R. J., Lundberg, R., & McKenzie, J. A. (2012). Dolomite-mediating bacterium isolated from the sabkha of abu dhabi (uae). *Terra Nova*, 3, 24.
- Bossart, P., Bernier, F., Birkholzer, J., Bruggeman, C., Connolly, P., & Dewonck, S. (2017). Mont Terri rock laboratory, 20 years of research: Introduction, site characteristics and overview of experiments. *Swiss Journal of Geosciences*, 110(1), 3–22.
- Boullia, S., Hinnov, L. A., & Huret, E. (2008). Astronomical calibration of the Early Oxfordian (Vocontian and Paris basins, France): Consequences of revising the Late Jurassic time scale. *Earth and Planetary Science Letters*, 276, 40–51.
- Brown, A. C. (1992). Sediment-host of stratiform copper deposits. *Geoscience Canada*, 19(3), 125–141.
- Campbell, F. A., & Williams, G. D. (1965). Chemical composition of shales of Mannville Group (Lower Cretaceous) of Central Alberta, Canada. *AAPG Bulletin*, 49(1), 81–87.
- Charles, N., Augier, R., Gumiaux, C., Monié, P., Chen, Y., Faure, M., & Zhu, R. (2013). Timing, duration and role of magmatism in wide rift systems: Insights from the Jiaodong Peninsula (China, East Asia). *Gondwana Research*, 24, 412–428.
- Chen, Z. P., Ren, Z. L., Yu, C. Y., Qi, K., Ren, W. B., Yang, Y., & Ma, J. (2018). Characteristics and genetic analysis of hydrothermal sediment of Lower Cretaceous in Hari Depression, Yin'e Basin. *Earth Science*, 43(06), 1941–1956. in Chinese with English Abstract.
- China Atomic Energy Authority, 2021. Construction of China's beishan underground research laboratory. Retrieved June 18, 2021 from http://m.stdaily.com/index/kejixinwen/2021-06/18/content_1157991.shtml
- Dai, C. C., Zheng, R. C., Wen, H. G., Lei, G. M., & Xie, C. H. (2008). Origin of lacustrine dolomite in Shahejie Formation from Liaodongwan Basin. *Journal of Chengdu University of Technology*, 35(2), 187–193. in Chinese with English Abstract.
- Davies, G. R., & Smith, L. B. (2006). Structurally controlled hydrothermal dolomite reservoir facies: An Overview. *AAPG Bulletin*, 90, 1641–1690.
- Distinguin, M., & Lavanchy, J. M. (2007). Determination of hydraulic properties of the Callovo-Oxfordian argillite at the Bure site: Synthesis of the results obtained in deep boreholes using several in situ investigation techniques. *Physics and Chemistry of the Earth*, 32, 379–392.
- Dou, L., & Chang, L. (2003). Fault linkage patterns and their control on the formation of the petroleum systems of the Erlan Basin, Eastern China. *Marine and Petroleum Geology*, 20, 1213–1224.
- Du, J. J., Qin, X. H., Zeng, Q. L., Zhang, L. Q., Chen, Q. C., Zhou, J., & Meng, W. (2017). Estimation of the present-day stress field using in-situ stress measurements in the alxa area, inner mongolia for china's hlw disposal. *Engineering Geology*, 220, 76–84. <https://doi.org/10.1016/j.enggeo.2017.01.020>
- Elderfield, H., & Greaves, M. J. (1982). The rare earth elements in seawater. *Nature*, 296(5854), 214–219.
- Faybishenko, B., Birkholzer, J., Sassani, D., & Swift, P. (2017). International Approaches for Nuclear Waste Disposal in Geological Formations: Geological Challenges in Radioactive Waste Isolation-Fifth Worldwide Review. Lawrence Berkeley National Laboratory, United States.
- Feng, M. Y., Wu, P. C., Qiang, Z. T., Liu, X. H., Duan, Y., & Xia, M. L. (2017). Hydrothermal dolomite reservoir in the Precambrian Dengying

- Formation of central Sichuan Basin, Southwestern China. *Marine and Petroleum Geology*, 82, 206–219.
- Gao, H. L., He, J. G., Zhang, S., Kong, W. H., Tian, M. M., & Huang, X. F. (2013). Study on crustal stability of Alashan area. *World Nuclear Geoscience*, 30(4), 237–244. (in Chinese with English Abstract).
- Gaucher, E. C., Robelin, C., Matray, J. M., Negrel, G., & Bouchet, A. (2004). Andra underground research laboratory: Interpretation of the mineralogical and geochemical data acquired in the Callovian-Oxfordian formation by investigative drilling. *Physics & Chemistry of the Earth Parts a/b/c*, 29(1), 55–77.
- IAEA. (2003). Scientific and Technical Basis for Geological Disposal of Radioactive Wastes. Technical Reports Series No. 413. International Atomic Energy Agency, Vienna, Austria, 80.
- Jones, B., & Manning, D. A. C. (1994). Comparison of geochemical indices used N for the interpretation of palaeo redox conditions in ancient mudstones. *Chemical Geology*, 111(111), 111–129.
- Klinkhammer, G. P., Elderfield, H., Edmond, J. M., & Mitra, A. (1994). Geochemical implications of rare earth element patterns in hydrothermal fluids from mid-ocean ridges-sciencedirect. *Geochim cosmochim acta*, 58(23), 5105–5113.
- Koeshidayatullah, A., Corlett, H., Stacey, J., Swart, P. K., Boyce, A., Robertson, H., Whitaker, F., & Cathy, H. (2020). Evaluating new fault-controlled hydrothermal dolomitization models: Insights from the Cambrian Dolomite, Western Canadian Sedimentary Basin. *Sedimentology: Journal of the International Association of Sedimentologists*, 67(6), 2945–2973.
- Li, H., Liu, Y. Q., Zhou, X., Niu, Y. Z., Li, X., & Liu, Y. J. (2017). Origin and geological significance of sedimentary exhalative rocks with “porphyritic” structures in the Middle Permian Pingdiquan Formation, eastern Junggar Basin. *Journal of Palaeogeography*, 19(2), 211–226. in Chinese with English Abstract.
- Li, H. B., Yang, J. S., Xu, Z. Q., Sun, Z. M., Tapponnier, P., & Van der Woerd, J. (2006). The Constraint of the Altyn Tagh Fault System to the Growth and Rise of the Northern Tibetan Plateau. *Earth Science Frontiers*, 13(4), 059–079226. in Chinese with English Abstract.
- Lin, C. S., Eriksson, K., Li, S. T., Wan, Y. X., Rem, J. Y., & Zhang, Y. M. (2001). Sequence architecture, depositional systems, and controls on development of lacustrine basin fills in part of the Erlan basin, northeast China. *AAPG Bulletin*, 85, 2017–2043.
- Liu, X. H., Duan, Y., Xia, M. L., Feng, M. Y., Wu, P. C., & Qiang, Z. T. (2017). Hydrothermal dolomite reservoir in the Precambrian Dengying Formation of central Sichuan Basin, Southwestern China. *Marine and Petroleum Geology*, 82, 206–219.
- Misaelides, P. (2019). Clay minerals and zeolites for radioactive waste immobilization and containment. In: *Modified Clay and Zeolite Nanocomposite Materials* (pp. 243–274). Amsterdam: Elsevier.
- Ould Bouaya, M. L. (2014). Acquisition d’un profil de perméabilité intrinsèque au sein de l’Argile à Opalines du Mont Terri par analyse minéralogique et pétrophysique. Master’s thesis, Université Paris-Sud 11, Orsay, France (in French).
- Pan, Z. Q., & Qian, Q. H. (2009). *Strategy research on high-level radioactive waste geological disposal* (pp. 15–17). Publishing House of Atomic Energy.
- Rao, Z., Li, G. R., Liu, X. D., Liu, P. H., Li, H. H., Liu, S., Zhu, M. Q., Guo, C., Ni, F. J., & Gong, Z. J. (2021). Fault activity in clay rock site candidate of high level radioactive waste repository, Tamusu Inner Mongolia. *Minerals*, 11(9), 941. <https://doi.org/10.3390/min11090941>
- Rao, Z., Liu, X. D., Liu, S., & Gong, Z. J. (2020). Optically stimulated luminescence dating analysis of Quaternary tectonic activity in Tamusu Candidate Area. *Science Technology and Engineering*, 20(25), 10170–10176. in Chinese with English Abstract.
- Scott, S. D. (1997). *Submarine Hydrothermal systems and deposits*. Wiley.
- Shi, Y. Q., Ji, H. C., Zhang, G. Y., Wang, J., Song, X. G., & Liu, J. X. (2021). Characteristics and genetic mechanisms of widely distributed zeolites in the Wutonggou Formation reservoir in the southern Junggar Basin. *Petroleum Science Bulletin*, 1, 1–15. <https://doi.org/10.3969/j.issn.2096-1693.2021.01.001>. in Chinese with English Abstract.
- SKB. (2004). R&D Programme 2004: Programme for Research, Development and Demonstration of Methods for the Management and Disposal of Nuclear Waste Including Social Science Research. TR-04–21. Swedish Nuclear Fuel and Waste Management Co. (SKB), Stockholm, Sweden, 412.
- Taylor, S. R., & McLennan, S. M. (1985). *The continental crust: Its composition and evolution*. Blackwell Scientific Publication.
- Wang, B. J. (2014). Characteristics and origin on the lacustrine dolostone of the Shahejie Formation in Tanggu area, Bohai Bay Basin. Dissertation, Nanjing University. (in Chinese)
- Wang J., Chen L., Su R. & Zhao X.G. (2018a) The Beishan underground research laboratory for geological disposal of high-level radioactive waste in China: planning, site selection, site characterization and in situ tests. *Journal of Rock Mechanics and Geotechnical Engineering*, 10, 411–435.
- Wang, F. G., Hou, S. R., Zhang, L., Meng, H. & Wang, J. L. (2018b). Study on the characteristics of water-rock interaction and its relation to uranium mineralization in Tamusu uranium deposit, southern Bayin Gobi Basin. *Geological Review*, 64, 633–646 (in Chinese with English abstract).
- Wang, Y., Liang, H. A., Hu, Q. B., Chen, H. K., Wang, C., & Xie, Z. (2018c). Study on correlation between mineral composition and elastic modulus of clay rock in Tamusu. *Chongqing Architecture*, 17, 18–21 (in Chinese with English abstract).
- Wang, T., Zhang, S. Y., Wei, P., Li, J. F., Guo, H., & Zhang, S. C. (2022). Genesis of zeolite minerals and its influences on reservoir properties. *Lithologic Reservoirs*, 34(1), 175–186. in Chinese with English Abstract.
- Wei, H. Y., & Jiang, X. C. (2019). Early Cretaceous ferruginous and its control on the lacustrine organic matter accumulation: Constrained by multiple proxies from the Bayingebi Formation in the Bayingebi Basin, Inner Mongolia, NW China. *Journal of Petroleum Science and Engineering*, 178, 162–179.
- Wen, H. G., Zheng, R. C., Qing, H. R., Fan, M. T., Li, Y. N., & Gong, B. S. (2014). Primary dolostone related to the Cretaceous lacustrine hydrothermal sedimentation in Qingxi Sag, Jiuquan Basin on the Northern Tibetan Plateau. *Science China: Earth Sciences*, 56(12), 2080–2093. in Chinese with English Abstract.
- Witherspoon, P. A., & Bodvarsson, G. S. (2001). *Geological challenges in radioactive waste isolation: Third worldwide review*. Lawrence Berkeley National Laboratory University of California.
- Wu, R. G., Zhou, W. P., Xu, Z., Liu, P. H., & Zhang, L. (2010). Discussion on the chronology of Suhongtu Formation in Bayingebi Basin. *Uranium Geology*, 26(3), 152–157. in Chinese with English abstract.
- Xiang, L., Liu, X. D., Liu, P. H., & Dai, C. C. (2019). Geochemical characteristics and its geological significance of lacustrine dolomitic mudstones in Yingejing depression, Inner Mongolia. *Geological Journal of China Universities*, 25(2), 221–231. in Chinese with English abstract.
- Xiang, L., Liu, X. D., Liu, P. H., Jiang, X. F., & Dai, C. C. (2020). Mineralogical and hydraulic characteristics of mudstone in the Tamusu candidate area in northwest China for high-level radioactive waste geological disposal purposes. *Clay Minerals*. <https://doi.org/10.1180/clm>
- Yu, H. D., Lu, C., Chen, W. Z., & Li, H. (2021). Permeability changes in fractured Tamusu mudstone in the context of radioactive waste disposal. *Bulletin of Engineering Geology and the Environment*, 80(10), 7945–7957.
- Yven, B., Sammartino, S., Geroud, Y., Homand, F., & Villieras, F. (2007). Mineralogy, texture and porosity of Callovo-Oxfordian argillites of the Meuse/Haute-Marne region (eastern Paris Basin). *Bulletin De La Societe Geologique De France*, 178, 73–90.
- Zhai, X. F., Wang, Z. C., Luo, P., Wang, T. S., Shi, S. Y., & Zhang, H. (2017). Characteristics and origin of microbial dolomite reservoirs in Upper Sinian Deinying Formation, Eastern Gaoshiti Area, Sichuan Basin, SW China. *Natural Gas Geoscience*, 28(8), 1199–1210. in Chinese with English Abstract.
- Zhang, C. L. (2018). Thermo-hydro-mechanical behavior of clay rock for deep geological disposal of high-level radioactive waste. *Rock Mechanics and Geotechnical Engineering*, 10, 992–1048.
- Zhang, K., Liu, R., Liu, Z. J., Li, L., Wu, X. P., & Zhao, K. G. (2020). Influence of palaeoclimate and hydrothermal activity on organic matter accumulation in lacustrine black shales from the Lower Cretaceous Bayingebi Formation of the Yin’e Basin, China. *Palaeogeography: Palaeoclimatology, Palaeoecology: An International Journal for the Geo-Sciences*. <https://doi.org/10.1016/j.palaeo.2020.110007>
- Zhang, C. Y., Nie, F. J., Jiao, Y. Q., Deng, W., Peng, Y. B., Hou, S. R., Dai, M. J., & Ye, T. F. (2019). Characterization of ore-forming fluids in the Tamusu sandstone-type uranium deposit, Bayingobi Basin, China: Constraints from trace elements, fluid inclusions and C–O–S isotopes. *Ore Geology Reviews: Journal for Comprehensive Studies of Ore Genesis and Ore Exploration*. <https://doi.org/10.1016/j.oregeorev.2019.102999>

- Zheng, R. C., Wen, H. G., Li, Y., & Chang, H. L. (2018). Compositions and texture of lacustrine exhalative rocks from the Lower Cretaceous Xiagou Formation in Qingxi Sag of Jiuxi Basin, Gansu. *Journal of Palaeogeography*, 20(1), 1–18. in Chinese with English Abstract.
- Zhong, D. K., Yang, Z., Sun, H. T., & Zhang, S. (2018). Petrological characteristics of hydrothermal-sedimentary rocks: A case study of the Lower Cretaceous Tengger Formation in the Baiyinchagan Sag of Erlian Basin, Inner Mongolia. *Journal of Paleogeography*, 20(1), 20–32. in Chinese with English Abstract.
- Zhou, J. B., Wilde, S. A., Zhang, X. Z., Ren, S. M., & Zheng, C. Q. (2011). Early Paleozoic metamorphic rocks of the Erguna block in the Great Xing'an Range, NE China: evidence for the timing of magmatic and metamorphic events and their tectonic implications. *Tectonophysics: International Journal of Geotectonics and the Geology and Physics of the Interior of the Earth*, 499, 105–117.
- Zhu, S., Cui, H., Jia, Y., Zhu, X. M., Tong, H., & Ma, L. C. (2020). Occurrence, composition, and origin of analcime in sedimentary rocks of non-marine petroliferous basins in China. *Marine and Petroleum Geology*. <https://doi.org/10.1016/j.marpetgeo.2019.104164>
- Zhu, S. F., Zhu, X. M., Wang, X. L., & Liu, Z. Y. (2012). Zeolite diagenesis and its control on petroleum reservoir quality of Permian in northwestern margin of Junggar Basin, China. *Science China Earth Sciences*, 55, 386–396. <https://doi.org/10.1007/s11430-011-4314-y>
- Zuo, Y. H., Qiu, N. S., Hao, Q. Q., Pang, X. Q., & Zhao, Z. Y. (2015). Geothermal regime and source rock thermal evolution in the Chagan sag, Inner Mongolia, northern China. *Marine and Petroleum Geology*. <https://doi.org/10.1016/j.marpetgeo.2014.09.001>

Publisher's Note

Springer Nature remains neutral with regard to jurisdictional claims in published maps and institutional affiliations.

Submit your manuscript to a SpringerOpen[®] journal and benefit from:

- Convenient online submission
- Rigorous peer review
- Open access: articles freely available online
- High visibility within the field
- Retaining the copyright to your article

Submit your next manuscript at ► [springeropen.com](https://www.springeropen.com)